

Joint Detection-Estimation of Brain Activity in Functional MRI: A Multichannel Deconvolution Solution

Salima Makni, Philippe Ciuciu, *Member, IEEE*, Jérôme Idier, and Jean-Baptiste Poline

© 2005 IEEE. Personal use of this material is permitted. However, permission to reprint/republish this material for advertising or promotional purposes or for creating new collective works for resale or redistribution to servers or lists, or to reuse any copyrighted component of this work in other works must be obtained from the IEEE.

Abstract—Analysis of functional magnetic resonance imaging (fMRI) data focuses essentially on two questions: first, a detection problem that studies which parts of the brain are activated by a given stimulus and, second, an estimation problem that investigates the temporal dynamic of the brain response during activations. Up to now, these questions have been addressed independently. However, the activated areas need to be known prior to the analysis of the temporal dynamic of the response. Similarly, a typical shape of the response has to be assumed *a priori* for detection purpose. This situation motivates the need for new methods in neuroimaging data analysis that are able to go beyond this unsatisfactory tradeoff. The present paper raises a novel detection-estimation approach to perform these two tasks simultaneously in region-based analysis. In the Bayesian framework, the detection of brain activity is achieved using a mixture of two Gaussian distributions as a prior model on the “neural” response levels, whereas the hemodynamic impulse response is constrained to be smooth enough in the time domain with a Gaussian prior. All parameters of interest, as well as hyperparameters, are estimated from the posterior distribution using Gibbs sampling and posterior mean estimates.

Results obtained both on simulated and real fMRI data demonstrate first that our approach can segregate activated and nonactivated voxels in a given region of interest (ROI) and, second, that it can provide spatial activation maps without any assumption on the exact shape of the Hemodynamic Response Function (HRF), in contrast to standard model-based analysis.

Index Terms—Bayesian analysis, detection-estimation, event-related fMRI, Gibbs sampling, HRF modeling, semi-blind deconvolution.

I. INTRODUCTION

THE overall aim of functional magnetic resonance imaging (fMRI) is to advance in the understanding of the relation between functions (cognitive or sensori-motor ones) and structure in the human brain. To this end, current fMRI paradigms consist of various stimulus types or conditions (visual, auditory, etc.) presented to the subject while brain volumes are acquired (typically every few seconds). Each stimulus induces a neuronal activation, which itself is responsible for some changes

of physiological parameters (blood flow, blood volume, deoxy-hemoglobin concentration, etc.) leading to a local increase of blood oxygenation, which is referred to as the blood oxygenated level-dependent (BOLD) effect [1].

The fMRI data can be analyzed using exploratory methods (Cluster analysis [2], [3], principal component analysis (PCA) [4], [5], and independent component analysis (ICA) [6], [7]), but the most popular approach is based on massively univariate (voxelwise) regression techniques implemented in many paradigms such as statistical parametric mapping (SPM) [8], the FMRIB Software Library (FSL), and Analysis of Functional Neuroimages (AFNI). In this latter framework, once a model has been specified, Student-*t* or Fisher statistics are calculated over the whole brain in order to identify the regions that are activated in response to a given contrast of experimental conditions. However, methods to estimate the temporal dynamic in brain regions have received less attention and have yet to be further developed in neuroimaging. In this paper, we propose to merge detection and estimation of the dynamic in one step in a Bayesian framework.

For detection purposes, a general linear time invariant (LTI) model, coding for the so-called *design matrix*, is built to assess the link between the fMRI data and the expected BOLD signal (regressors) in any voxel of the brain. Typically, each column of this matrix defines a *regressor*, which is computed as the convolution of a specific stimulus sequence with an *a priori* Hemodynamic Response Function (HRF), modeling the impulse response of the neurovascular system.

Once the brain activity has been well localized for every contrast of interest, analysis of the HRF shape may help to understand the dynamic of the physiological process in terms of activation delay (time to peak), undershoot, and putative initial dip [9]. Over the last few years, a great deal of attention has been paid to the development of voxel-wise methods for HRF estimation. Recently, a nonlinear differential equation system (i.e., the Balloon model) has been proposed to explain the hemodynamics changes based on the mechanically compelling model of an expandable venous compartment [10] and the standard Windkessel theory [11]. Several studies have proposed a state-space equation framework first to identify the parameters of such nonlinear models and, second, to predict nonlinearities in the BOLD response [12], [13]. Assuming a nonlinear model between the fMRI time course and the stimulus sequence is necessary to account specially for a *refractory* period that may occur when the interstimulus interval (ISI) is shorter than 1 s. As shown in [12], other hemodynamic nonlinearities may also

Manuscript received September 30, 2004; revised April 5, 2005. This work was supported in part by the French Ministry of Research (ACI Cognition et Traitement de l'Information). The associate editor coordinating the review of this manuscript and approving it for publication was Guest Editor Dr. Keith Worsley.

S. Makni, P. Ciuciu, and J.-B. Poline are with Service Hospitalier Frédéric Joliot (CEA), 91406 Orsay, Cedex, France and with IFR 49, Paris, France (e-mail: name@shfj.cea.fr).

J. Idier is with Institut de Recherche en Communications et Cybernétique de Nantes (IRCCyN/CNRS), 44321 Nantes, Cedex 3, France (e-mail: Jerome.Idier@ircyn.ec-nantes.fr).

Digital Object Identifier 10.1109/TSP.2005.853303

appear at about 8 sec poststimulus, which are attributed to a high deoxyhemoglobin concentration during the flow undershoot following the first stimulus. Nonetheless, most of fMRI studies rely on an experimental design that makes the exploration of BOLD nonlinearities unreachable. In such cases, linear modeling constitutes a simpler and satisfactory approximation of the BOLD dynamics, especially when the ISI is more than 2 s.

Pioneering works have embedded parametric models of the HRF shape in a linear framework [14]–[16], [21]. Fitting the parameters in the least square sense has provided an easy way to get the dynamic of the response [16], [17], [21]. Nonetheless, fMRI modeling requires flexibility since the HRF may vary from region to region, task to task, and subject to subject [18]–[20]. Flexibility in parametric linear models has been achieved through the use of a function basis [21], [22]. However, the function basis set imposes a hard constraint on the detectable HRF shapes. To overcome these problems, more adaptive parametric models have been introduced first for fixed epoch fMRI experiments [23], [24]. Recently, these works have been extended to any kind of fMRI experiment in [25]. In this contribution, Woolrich and colleagues have generalized the HRF parameterization of [23] using a half-cosine basis, allowing isolation of different shape characteristics of the HRF. Other contributors have considered nonparametric formulations [26]–[29] in the Bayesian setting and, more specifically, in a state-space framework [30], [31]. All these studies impose a temporal constraint on the regularity of the HRF since the underlying physiological process is slow-varying in time.

A strong limitation that arises in the above-mentioned methods is their lack of robustness, mainly due to the low signal-to-noise ratio (SNR). HRF estimation turns out to be reliable only in high SNR voxels. To increase this ratio, one solution consists of pooling voxels. However, this procedure still requires to select voxels with high SNR values. This can be achieved using testing procedures with constraint models for HRF. On the other hand, two noticeable features have been pointed out [28], [29]. First, for a given stimulus type, the shape of the HRF tends to be spatially homogeneous. Second, the fluctuation of the HRF estimate from one condition to another in a given voxel essentially relies on a *magnitude modulation*. To account for these features in an efficient and robust way, we have derived a region-based formulation of the HRF estimation problem in [32]. In this latter work, we have characterized the vasculature of a given region of interest (ROI) by a single HRF shape but allowed for variation in the magnitude of the response. We have also introduced stimulus-dependent magnitude coefficients for each voxel of a ROI to model the *space-varying* response level to a given stimulus type. This coefficient defines a pseudo-neural response and may better represent the actual “neural” response level (NRL), as seen by deconvolution of the BOLD response [13]. A noticeable limitation of [32] is that the average activity is computed from all the voxels in a ROI. However, for a given region, some voxels may not be activated for one or several conditions. Therefore, in this paper, we develop a new formulation that allows us to perform the detection and estimation steps at the same time. As explained further, this model, which is embodied in a Bayesian approach, is able to segregate activated voxels within a region from nonactivated ones.

Following [27] and [28], the HRF is assumed to be a slowly time-varying function using a Gaussian prior distribution. The NRLs are supposed to be statistically independent from one stimulus type to another. In this work, no spatial correlation is introduced between pseudo-neural responses in nearby voxels because such a model should be based on measured activity, and until now, it is not clear what correlation will be observed. In any case, such a spatial model would preferably be considered on cortical geodesic distance rather than on voxel Euclidean distance. Akin to [33] and [34], in order to solve for the detection of activated voxels in response to a given condition, we consider a two-class Gaussian mixture as a prior probability density function (pdf) on the NRLs. For any condition of interest, the role of the mixture is to efficiently discriminate activating areas from not activating ones in the ROI. Modeling the deactivation process is beyond the scope of this paper, but it could be addressed in the future using a third class in the mixture (see, for instance, [33]).

All parameters of interest (the HRF and the NRLs), as well as hyperparameters, which govern the prior laws, and space-varying parameters (the deterministic trend due to physiological artifacts and the noise variances) should be estimated in an appropriate way. To this end, a Bayesian joint detection-estimation approach is proposed, as explained in the following.

The rest of the paper is organized as follows. Section II revisits the LTI voxelwise modeling of the HRF proposed in [28]. Some notations that will be used throughout the paper are also introduced in this section. Section III focuses on the modeling of fMRI signal across voxels in a given ROI. In Section IV, we present how detection-estimation can be jointly performed. Section V provides the main steps of our Gibbs sampling algorithm. Section VI illustrates the performances of our approach on synthetic data in comparison with previous works [27], [28]. In Section VII, the behavior of our method is analyzed on experimental fMRI data. In Section VIII, we discuss the possible extensions of the proposed method.

II. VOXELWISE FORMULATION

A. Notations

The notations used in this paper are summarized in Table I. In what follows, all vectors are considered as columns by default. Moreover, we will use the notation $\ell = m : n$ as a shorthand for $\ell = m, \dots, n$.

B. LTI System

Let us define $\mathbf{y}_j = (y_{j,t_n})_{n=1:N}$ as the BOLD fMRI time course measured in voxel V_j at (not necessarily uniformly sampled) times t_n , and define $(x_{t_n}^m)_{n=1:N}$ as the corresponding binary vector for the m th condition: $x_{t_n}^m = 1$ if t_n is an onset (i.e., an arrival time) for the m th condition. In classical voxel-dependent approaches [28], [35], a convolution model is assumed between the stimuli and the data

$$y_{j,t_n} = \sum_{m=1}^M \sum_{d=0}^D h_{j,d\Delta t}^m x_{t_n}^m - d\Delta t + \sum_{q=1}^Q p_{t_n,q} \ell_{q,j} + b_{j,t_n}.$$

TABLE I
LIST OF NOTATIONS

$\mathbf{y}_j \in \mathbb{R}^N$	Data fMRI time series acquired in voxel V_j
$\mathbf{y} = [\mathbf{y}_1, \dots, \mathbf{y}_J]$	Matrix of size $N \times J$ representing fMRI time series acquired in all voxels of the ROI
$\mathbf{b}_j \in \mathbb{R}^N$	Gaussian noise vector in voxel V_j
$D + 1$	Number of HRF coefficients
\mathbf{X}^m	Binary ‘‘onsets matrix’’ of the m th condition of size $N \times (D + 1)$
\mathbf{h}	HRF to be estimated
M	Number of different conditions in the experiment
a_j^m	NRL for voxel V_j and condition m
Q	Number of drift parameters
$\mathbf{P} = [\mathbf{p}_1, \dots, \mathbf{p}_Q]$	Low frequency orthogonal matrix of size $N \times Q$
$\boldsymbol{\ell}_j \in \mathbb{R}^Q$	Nuisance parameter vector for voxel V_j
ϵ_j^2	Noise variance for voxel V_j
$\boldsymbol{\lambda} = (\lambda_{1,m})_{m=1:M}$	Vector of the weighting probabilities
$\mu_{1,m}$	Mean value of NRLs for activated voxels in condition m
$\sigma_{1,m}^2$	Variance of NRLs for activated voxels in condition m
$\sigma_{0,m}^2$	Variance of NRLs for nonactivated voxels in condition m
$C_{1,m}$	$J_{1,m}$ -dimensional vector of activated voxel indexes in condition m
$C_{0,m}$	$J_{0,m}$ -dimensional vector of nonactivated voxel indexes in condition m

Vector $\mathbf{h}_j^m = (h_{j,d\Delta t}^m)_{d=0:D}$ represents the unknown HRF in voxel V_j corresponding to the m th condition. In matrix form, this relation reads

$$\mathbf{y}_j = \sum_{m=1}^M \mathbf{X}^m \mathbf{h}_j^m + \mathbf{P}\boldsymbol{\ell}_j + \mathbf{b}_j \quad (1)$$

where $\mathbf{X}^m = (x_{t_n-d\Delta t}^m)_{n=1:N,d=0:D}$ is a $N \times (D + 1)$ binary matrix corresponding to the arrival times for the m th condition. Equation (1) is the sum of three terms.

- The first one represents the stimulus-induced BOLD signal. More precisely, each term $\mathbf{X}^m \mathbf{h}_j^m$ represents the activation response in voxel V_j to condition m .
- $\mathbf{P}\boldsymbol{\ell}_j$ is the confounds part (deterministic trends).
- \mathbf{b}_j models the noise term.

The goal of our method is to extract the first term from the other two. In the next paragraphs, we describe our assumptions for each of these two terms.

C. Drift Model

In neuroimaging experiments, the fMRI data are contaminated by a low-frequency drift, mainly due to physiological artifacts [36]. Breathing and cardiac pulses are aliased since the sampling frequency of the data is below Nyquist’s bound. A highpass filter is generally used to remove these trends before estimating the HRF. These baseline techniques are merely pre-processing steps to eliminate drifts in the fMRI data. A relevant alternative was also proposed in a semi-parametric framework [37] and is adopted in this paper to model the trend. This approach relies on matrix $\mathbf{P} = [\mathbf{p}_1, \dots, \mathbf{p}_Q]$ (Q depends on the lowest frequency attributable to the drift term), which consists of an orthonormal basis of functions $\mathbf{p}_q = (p_q(t_n))_{n=1:N}$. To each voxel is attached an unknown weighting vector $\boldsymbol{\ell}_j$.

D. Noise Model

Several temporal noise models may be considered. For a given ROI \mathcal{R} , the simplest noise model is a zero-mean Gaussian white process \mathbf{b} of unknown variance ϵ^2 , independent

of \mathbf{h} ($\mathbf{b} \sim \mathcal{N}(\mathbf{0}, \epsilon^2 \mathbf{I})$). Nonetheless, it is well known that fMRI time series are correlated in time [38]. Several authors have proposed to estimate the temporal covariance matrix of the noise using an autoregressive model [39], [40]. In [41], a *spatially varying first-order* AR model has been considered. In the present paper, we will only consider a *spatially varying* white noise model since it was actually demonstrated in [42] that various noise correlation structures have little influence on the performances of the HRF estimation. This means that a specific noise variance ϵ_j^2 is assigned to each voxel V_j , allowing for spatially varying artifacts (such as the partial volume effect) to be treated in an appropriate way. Hence, we will need to estimate vector $\boldsymbol{\epsilon}^2 = (\epsilon_j^2)_{j=1:J}$ of noise variances.

III. PROPOSED REGIONAL MODEL

A. Motivation

In [28], the authors have described a method for voxel-specific HRF estimation or, more generally, from a given time series in the context of event-related paradigms. This approach only focused on the temporal aspects, i.e., spatial features were not considered. Results of this method on actual fMRI data showed that HRF estimates, which are computed in neighbor voxels, have approximately the same shape up to a magnitude factor. This property of shape similarity was also observed, in numerous cases, for HRF estimates computed in the same voxel but for different stimulus types [28], [29]. However, in some experimental paradigms such as repetition-suppression ones, because of the habituation phenomenon, estimated HRFs in neighbor voxels may show differences with respect to (w.r.t.) the activation delay or the peak intensity.

Brain regions activated by a given stimulus usually spread over a number of contiguous voxels. A study of the response over an homogeneous region seems therefore reasonable. This region could be defined anatomically or functionally by some brain parcellation technique [43] or clustering algorithm [44].

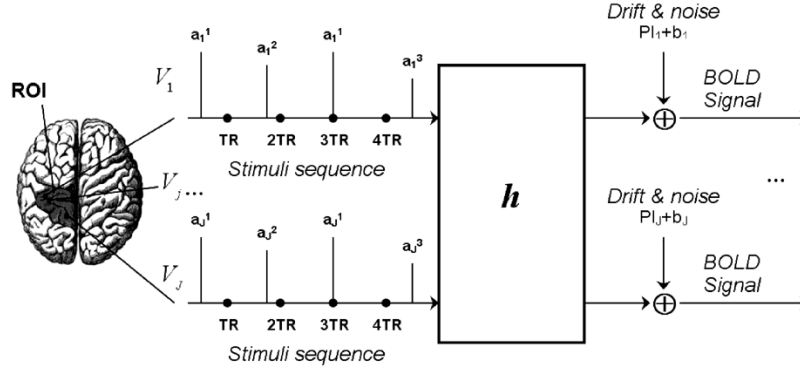


Fig. 1. ROI-based model. \mathbf{h} is the single HRF for all the voxels of the ROI. a_j^m defines the NRL for voxel V_j and stimulus type (or condition) m .

B. Assumptions

- ($\mathcal{H}1$) We consider a LTI model.
- ($\mathcal{H}2$) We assume that the fMRI time series $\mathbf{y} = [\mathbf{y}_1, \dots, \mathbf{y}_J]$ are statistically independent and identically distributed (i.i.d.) in space. We also consider that there is no noise correlation in space.
- ($\mathcal{H}3$) We do not model any spatial correlation between the NRLs of neighbor voxels. In the recent litterature, several contributions have introduced spatial priors either on the *activation height* [24], [45] or on the labels of the classes associated with the mixture model [46], [47]. This latter idea seems relevant to remove isolated false positives since it encodes the prior belief that neighboring voxels are likely to belong to the same class. We could also extend our model to spatial mixtures that should be preferably defined on the cortical surface using a two-dimensional (2-D) Markov random field.
- ($\mathcal{H}4$) Generally, fMRI experiments consist of several conditions (visual, auditory, etc.). We assume that the responses to different stimuli combine in a *linear* way.

C. Problem Statement

Once an homogeneous ROI is defined, our purpose is to estimate its *canonical* time response. More precisely, we characterize the ROI by a single HRF shape and a magnitude coefficient for each voxel and stimulus type. It is likely that this coefficient may better represent the NRL. To this end, we introduce a special case of (1) that accounts for stimulus/voxel-dependent signal and voxel-dependent noise levels but assumes a single HRF shape over the region. Letting $\mathcal{R} = (V_j)_{j=1:J}$ be the ROI, then (1) reads

$$\mathbf{y}_j = \sum_{m=1}^M a_j^m \mathbf{X}^m \mathbf{h} + \mathbf{P}\ell_j + \mathbf{b}_j, \quad \forall j = 1 : J \quad (2)$$

where a_j^m stands for the NRL in voxel V_j for condition m . Fig. 1 summarizes the main features of model (2).

IV. A PRIORI MODEL AND THE DETECTION/ESTIMATION PROBLEM

Assuming that a given region has homogeneous vasculature properties, we propose to estimate the corresponding HRF and

to simultaneously classify voxels in the ROI as either activating or not activating. This classification task has already been applied to fMRI data either using a nonspatial mixture model [34] or a spatial one [33], [46], [47]. Following [34], we introduce a two-class mixture model: one for activated voxels (class 1) and the other for nonactivated ones (class 0). In this framework, we need to estimate the label attached to each voxel of the ROI and the corresponding NRL. Since this model stands for a given stimulus type, we consider M two-class mixtures, each of them being coupled to a single stimulus type.

The estimation of the NRLs and the HRF may be thought of as a multichannel, semi-blind deconvolution problem. Indeed, the different channels correspond to the available voxels and “semi-blind” refers to the prior knowledge of the arrival times of the “neural” responses. In contrast, arrival times have to be identified as well in some other applications of sparse spike deconvolution such as geophysics [48]. For all parameters of interest, the respective *a priori* models are described in the following.

A. HRF

As physiologically advocated in [49], the HRF can be characterized as follows [28], [35]:

- i*) Its temporal variations are smooth. Quantification is achieved by setting Gaussian prior for the norm of the second derivative of the HRF, whose variance is adjusted by hyperparameter $\sigma_{\mathbf{h}}^2$. More precisely, we assume $\mathbf{h} \sim \mathcal{N}(\mathbf{0}, \|\partial^2 \mathbf{h}\|^2 / (2\sigma_{\mathbf{h}}^2))$. Following usual practice, $\|\partial^2 \mathbf{h}\|^2$ can be discretized as

$$(\partial^2 \mathbf{h})_{d\Delta t} \approx \frac{h_{(d+1)\Delta t} - 2h_{d\Delta t} + h_{(d-1)\Delta t}}{(\Delta t)^2} \quad \forall d = 1 : D - 1.$$

Taking into account (*i*), we obtain in matrix form $\partial^2 \mathbf{h} = \mathbf{D}_2 \mathbf{h}$, where \mathbf{D}_2 is the *truncated* second-order finite difference matrix of size $(D - 1) \times (D - 1)$ that depends on Δt [35]. Hence, $\|\partial^2 \mathbf{h}\|^2 = \mathbf{h}^t \mathbf{R}^{-1} \mathbf{h}$, where $\mathbf{R} = (\mathbf{D}_2^t \mathbf{D}_2)^{-1}$ is symmetrical positive definite.

- ii*) It is causal, and its amplitude vanishes at the first and the end time points ($h_0 = h_{D\Delta t} = 0$), which corresponds to a duration of about 25 s.

Furthermore, akin to [50], we impose a normalization constraint i.e., $\mathbf{h} = 1$, to remove the scale ambiguity encountered in blind deconvolution problems [48].

B. “Neural” Response Levels

According to (H3), we have $p(\mathbf{a}; \boldsymbol{\theta}_m) = \prod p(\mathbf{a}^m; \boldsymbol{\theta}_m)$ with $\mathbf{a} = [\mathbf{a}^1, \dots, \mathbf{a}^M]$, $\mathbf{a}^m = (a_j^m)_{j=1:J}$, and $\boldsymbol{\theta}_m = (\boldsymbol{\theta}_m)_{m=1:M}$, where vector $\boldsymbol{\theta}_m$ gathers the hyperparameters related to the prior pdf of the NRLs for the m th stimulus type. These hyperparameters are unknown and will be further specified.

In some cases, a few voxels of the ROI are activated by a given condition, whereas others may not be. We therefore consider couples of random variables $z_j^m = (q_j^m, a_j^m)$, $j = 1 : J, m = 1 : M$. Parameter q_j^m is a binary random variable that indicates whether voxel V_j is activated or not by condition m (respectively, $q_j^m = 1$ or $q_j^m = 0$). Conditional on q_j^m , a_j^m is a Gaussian random variable that represents the NRL for voxel V_j and condition m . To model this prior knowledge about the activation process, we introduce a two-class Gaussian mixture prior distribution

$$\lambda_{1,m} \mathcal{N}(\mu_{1,m}, \sigma_{1,m}^2) + \lambda_{0,m} \mathcal{N}(0, \sigma_{0,m}^2) \quad (3)$$

where $\forall j \in \{1, \dots, J\}$, $\lambda_{1,m} = \Pr(q_j^m = 1)$, and $\lambda_{0,m} = 1 - \lambda_{1,m}$. According to (H3), $\lambda_{1,m}$ is a condition-dependent factor, but it is not voxel-dependent.

As implied by (3), we attribute a Gaussian prior model to the NRLs

$$\begin{aligned} p(a_j^m | q_j^m = 1) &\sim \mathcal{N}(\mu_{1,m}, \sigma_{1,m}^2) \\ p(a_j^m | q_j^m = 0) &\sim \mathcal{N}(0, \sigma_{0,m}^2). \end{aligned}$$

Note that we set $\mu_{0,m} = 0$ since this parameter represents the mean of the amplitude levels for nonactivated voxels, which, by definition, should be zero. Thus, four hyperparameters describe this mixture prior model for each condition: $\boldsymbol{\theta}_m = [\lambda_{1,m}, \mu_{1,m}, \sigma_{1,m}^2, \sigma_{0,m}^2]$. Such a model is a generalization of the Gaussian prior distribution for the NRL's advocated in [32].

C. Low-Frequency Drift

Vector $\boldsymbol{\ell} = [\ell_1, \dots, \ell_J]$ gathers the unknown regression coefficients of the function basis \mathbf{P} . We assume that $\boldsymbol{\ell}$ is a random vector independent of \mathbf{h} , such that $p(\boldsymbol{\ell}; \boldsymbol{\tau}_\ell^2) = \prod_j p(\ell_j; \tau_\ell^2)$ and $\ell_j \sim \mathcal{N}(0, \tau_\ell^2 \mathbf{I}_Q)$. In this paper, the calculations will be provided in the noninformative case, that is, when $\tau_\ell^2 \rightarrow +\infty$. In

this case, the prior pdf becomes flat, which simplifies the expression of the full posterior pdf after integrating the drift parameters $\boldsymbol{\ell}$ out (see Section V).

D. Hyperparameters

The complete set of hyperparameters to be estimated is denoted $\boldsymbol{\Theta} = [\boldsymbol{\epsilon}^2, \sigma_{\mathbf{h}}^2, \boldsymbol{\theta}_m]$. For all these parameters, we resort to noninformative Jeffreys priors that meet the *reparametrization-invariance* requirement [51, p. 132]

$$\begin{aligned} p(\boldsymbol{\epsilon}^2) &= \prod_j p(\epsilon_j^2) = \prod_j \epsilon_j^{-1}, \quad p(\sigma_{\mathbf{h}}^2) = \sigma_{\mathbf{h}}^{-1} \\ p(\boldsymbol{\theta}_m) &= \prod_m p(\boldsymbol{\theta}_m) \\ &= \prod_m p(\lambda_{1,m}) p(\mu_{1,m}, \sigma_{1,m}^2) p(\sigma_{0,m}^2), \\ p(\lambda_{1,m}) &\propto \mathcal{B}(1/2, 1/2) \\ p(\mu_{1,m}, \sigma_{1,m}^2) &= \sigma_{1,m}^{-1}, \quad p(\sigma_{0,m}^2) = \sigma_{0,m}^{-1}. \end{aligned}$$

V. ALGORITHM

A. Likelihood

According to (H1)–(H2), the likelihood function reads

$$\begin{aligned} p(\mathbf{y} | \mathbf{h}, \mathbf{a}, \boldsymbol{\ell}, \boldsymbol{\epsilon}^2) &= \prod_j p(\mathbf{y}_j | \mathbf{h}, \mathbf{a}, \ell_j, \epsilon_j^2) \\ &\propto \left(\prod_j \epsilon_j^{-N} \exp\left(-\frac{1}{2\epsilon_j^2} \|\tilde{\mathbf{y}}_j - \mathbf{P}\boldsymbol{\ell}_j\|^2\right) \right) \end{aligned}$$

where $\tilde{\mathbf{y}}_j = \mathbf{y}_j - \sum_m a_j^m \mathbf{X}^m \mathbf{h}$. Maximum likelihood (ML) estimation of (\mathbf{h}, \mathbf{a}) is a bilinear inverse problem since (2) is linear w.r.t. \mathbf{h} when \mathbf{a} is fixed and *vice-versa*. In addition, the ML solution $(\mathbf{h}^*, \mathbf{a}^*)$ is not unique. For instance, every couple $(\mathbf{h}^*/C, \mathbf{a}^* \times C)$ defines another pair of solutions in the ML sense. By contrast, structural prior information is available both on \mathbf{h} and \mathbf{a} . Therefore, we resort to the Bayesian framework.

B. Joint Posterior Distribution

Considering the constructed model [cf. (H1)–(H4)] and assuming no further prior dependence between parameters, formal application of the chain rule yields (4), shown at the bottom of the page.

Since (2) is linear w.r.t. vectors $\boldsymbol{\ell}_j$ of nuisance variables, they can be easily integrated out. We therefore focus on the marginal distribution $p(\mathbf{h}, \mathbf{a}, \boldsymbol{\Theta} | \mathbf{y}) = \int p(\mathbf{h}, \mathbf{a}, \boldsymbol{\ell}, \boldsymbol{\Theta} | \mathbf{y}) d\boldsymbol{\ell}$ in order to get

$$\begin{aligned} p(\mathbf{h}, \mathbf{a}, \boldsymbol{\ell}, \boldsymbol{\Theta} | \mathbf{y}) &\propto p(\mathbf{y} | \mathbf{h}, \mathbf{a}, \boldsymbol{\ell}, \boldsymbol{\epsilon}^2) p(\mathbf{h}) p(\boldsymbol{\ell}) \left(\prod_m \prod_j \sum_{i=0}^1 p(a_j^m | q_j^m = i, \boldsymbol{\theta}_m) p(q_j^m = i) \right) p(\boldsymbol{\epsilon}^2) p(\sigma_{\mathbf{h}}^2) p(\boldsymbol{\theta}_m) \\ &\propto \left(\prod_j \epsilon_j^{-N-1} \right) \sigma_{\mathbf{h}}^{-D} \exp\left(-\frac{\mathbf{h}^t \mathbf{R}^{-1} \mathbf{h}}{2\sigma_{\mathbf{h}}^2} - \sum_j \frac{\|\tilde{\mathbf{y}}_j - \mathbf{P}\boldsymbol{\ell}_j\|^2}{2\epsilon_j^2}\right) \prod_m \left(p(\boldsymbol{\theta}_m) \prod_j \sum_{i=0}^1 \frac{\lambda_{i,m}}{\sigma_{i,m}} \exp\left(-\frac{(a_j^m - \mu_{i,m})^2}{2\sigma_{i,m}^2}\right) \right). \quad (4) \end{aligned}$$

fewer parameters to sample. Moreover, due to the Rao-Blackwellization property [52], the marginalization step reduces the variance of the remaining parameters to be sampled and yields

$$p(\mathbf{h}, \mathbf{a}, \Theta | \mathbf{y}) \propto \sigma_{\mathbf{h}}^{-D} \exp \left(-\frac{1}{2\sigma_{\mathbf{h}}^2} \mathbf{h}^t \mathbf{R}^{-1} \mathbf{h} - \frac{1}{2} \sum_j \tilde{\mathbf{y}}_j^t \mathbf{Q}_j \tilde{\mathbf{y}}_j \right) \times \prod_j \left(\epsilon_j^{Q-N-1} \prod_m \sum_{i=0}^1 \frac{\lambda_{i,m}^2 \lambda_{1-i,m}}{\sigma_{i,m}^2 \sigma_{1-i,m}} \right) \times \exp \left(-\frac{(a_j^m - \mu_{i,m})^2}{2\sigma_{i,m}^2} \right)$$

where $\mathbf{Q}_j = \epsilon_j^{-2}(\mathbf{I}_N - \mathbf{P}\mathbf{P}^t)$, and the orthogonality of \mathbf{P} (i.e., $\mathbf{P}^t\mathbf{P} = \mathbf{I}_N$) has been accounted for. As mentioned earlier in Section IV-C, choosing an informative prior for ℓ would have modified the term $\prod_j \epsilon_j^{Q-N-1}$ in $p(\mathbf{h}, \mathbf{a}, \Theta | \mathbf{y})$, making its sampling w.r.t. noise variances more tricky.

Due to the bilinearity of model (2) w.r.t. \mathbf{h} and \mathbf{a} , we do not consider the maximum *a posteriori* (MAP) estimate of (\mathbf{h}, \mathbf{a}) . Indeed, its computation would require stochastic optimization since $p(\mathbf{h}, \mathbf{a}, \Theta | \mathbf{y})$ may possess many local maxima. ‘‘Joint MAP’’ estimation has already been addressed in blind deconvolution problems with fixed hyperparameters [53], [54], but the proposed method suffers from shortcomings w.r.t. local minima and nonuniqueness of the solution. More importantly, the issue of hyperparameter tuning would not be easily addressed using the MAP approach. In fact, it was shown that simultaneous signal estimation and hyperparameter identification is achieved in this framework by maximizing the generalized likelihood whose maximizer is not statistically consistent [55]. Considering all aspects of this problem, we rather choose to compute an estimate of the posterior mean of the unknown parameters as well as the hyperparameters. Direct sampling from the joint posterior pdf is impossible. Therefore, we resort to Monte Carlo Markov chain methods [52] and, more specifically, to Gibbs sampling for which the full conditional pdfs needs to be derived.

C. Numerical Inference Using Gibbs Sampling

Gibbs sampling has already been applied in the context of blind deconvolution problems [48]. It consists of starting with a seed vector and sequentially modifying one (scalar or multidimensional) component at a time by sampling according to the full conditional pdf of that component given the remaining variables (denoted as rest in the following) and the data. Samples are composed of the set of all vectors whose components have been updated an equal amount of iterations.

A key issue with Gibbs sampling is to partition the vector of parameters into blocks whose full conditional sampling can be performed easily. In our case, we exploit the bilinearity of model (2) w.r.t. \mathbf{h} and \mathbf{a} that makes the full conditional pdfs $p(\mathbf{h} | \mathbf{y}, \mathbf{a}, \Theta)$ and $p(\mathbf{a} | \mathbf{y}, \mathbf{h}, \Theta)$ Gaussian, given the noise model and the priors. Then, the derivation of the full conditional pdfs corresponding to the chosen clustering is straightforward. As detailed in Table II, the updating

TABLE II
STEPS OF THE GIBBS SAMPLING ALGORITHM

-
- Setting up: choose $\mathbf{h}^0, \mathbf{a}^0, \lambda^0, (\epsilon^2)^0, \theta_{\mathbf{a}}^0$.
 - Iteration k : draw samples $\mathbf{h}^k, \mathbf{a}^k, \lambda^k, (\epsilon^2)^k, \theta_{\mathbf{a}}^k$ from the full conditional posterior pdfs:
 - HRF: $\mathbf{h}^k \sim p(\mathbf{h}^k | \mathbf{y}, \mathbf{a}^{k-1}, (\epsilon^2)^{k-1})$, cf. Eq. (7).
 - HRF scale: $(\sigma_{\mathbf{h}}^2)^k \sim p((\sigma_{\mathbf{h}}^2)^k | \mathbf{h}^k)$, cf. Eq. (8).
 - NRLs: for every condition m and every voxel j ,
 - * $(u_j^m)^k \sim \mathcal{U}[0, 1]$; if $(u_j^m)^k \leq (\lambda_{i,j}^m)^k$, then $(q_j^m)^k = 1$ otherwise $(q_j^m)^k = 0$.
 - * $(\sigma_j^m)^k | (q_j^m)^k = i \sim \mathcal{N}((\mu_{i,j}^m)^k, ((\sigma_{i,j}^m)^2)^k)$, $(i = 0, 1)$, cf. Eq. (9).
 - Noise variances: for every voxel j , $(\epsilon_j^2)^k \sim p((\epsilon_j^2)^k | \mathbf{y}_j, \mathbf{h}^k, \mathbf{a}_j^k)$, cf. Eq. (11).
 - Mixture parameters: for every condition m ,
 - * Weighting probability: $\lambda_{i,m}^k \sim p(\lambda_{i,m}^k | \mathbf{y}, \mathbf{h}^k, \mathbf{a}^k, (\epsilon^2)^k)$, cf. Eq. (12).
 - * Variance of NRLs for nonactivated voxels: $(\sigma_{0,m}^2)^k \sim p((\sigma_{0,m}^2)^k | \eta_{0,m}^k, \nu_{0,m}^k)$, cf. Eq. (13).
 - * Variance of NRLs for activated voxels: $(\sigma_{1,m}^2)^k \sim p((\sigma_{1,m}^2)^k | \eta_{1,m}^k, \nu_{1,m}^k)$, cf. Eq. (14).
 - * Mean of NRLs for activated voxels: $(\mu_{1,m})^k \sim p((\mu_{1,m})^k | (\sigma_{1,m}^2)^k, \eta_{1,m}^k, \nu_{1,m}^k)$, cf. Eq. (15).
 - Iterate until maximum iteration number K_0 is achieved. Finally, we compute posterior mean estimates using the following approximation (Samples $\theta^1, \dots, \theta^I$ are discarded: they correspond to the so-called *burn-in* period):

$$\hat{\theta}^{\text{PM}} = \frac{1}{K_1} \sum_{k=I}^{K_0} \theta^k, \quad K_1 = K_0 - I + 1, \quad \forall \theta \in \{\mathbf{h}, \mathbf{a}, \Theta\}$$

steps are performed on the following unknown variables: $\mathbf{h}, \sigma_{\mathbf{h}}^2, z_j^m = (q_j^m, a_j^m), \epsilon_j^2, \lambda_m, \sigma_{0,m}^2, \sigma_{1,m}^2$, and $\mu_{1,m}$. We therefore need access to the corresponding full conditional pdfs whose closed forms are given in Appendix A.

Once the Gibbs sampler has converged, these quantities are approximated by their sample counterparts, as emphasized in Table II. To check the convergence of our algorithm, we have plotted the values of several scalar parameters (a noise variance as well as other hyperparameters) w.r.t. iterations. Once the relative norm of these parameters is lower than a given threshold ($\alpha = 10^{-3}$), it was decided that the sampling scheme could stop. Following [29], we could implement more sophisticated convergence diagnosis if necessary. However, in practice, we did not experience convergence problems.

VI. SIMULATION RESULTS

A. Generation of Synthetic Datasets

We simulated a *random-intermixed* sequence of indexes coding for two different stimulus types ($M = 2$). Each index m corresponded to a specific stimulus. The timing of the trials was random since the retained inter-stimulus intervals (ISIs) were uniformly distributed on [1.5, 2.5] sec. For such ISI values, the linear approximation of the response is valid. For the simulation, we also took one session of $N = 100$ time points (e.g., scan number). The sampling interval δt of the trial onsets was set to 0.5 s. The onsets arrival times are put in the $n\delta t$ grid by moving them to the nearer time points on this grid.

The ROI \mathcal{R} consisted of $J = 60$ voxels. As indicated in Table I, $C_{1,m}$ and $C_{0,m} = \mathcal{R} \setminus C_{1,m}$ are the sets of activated and nonactivated voxels in \mathcal{R} for condition m , respectively. For

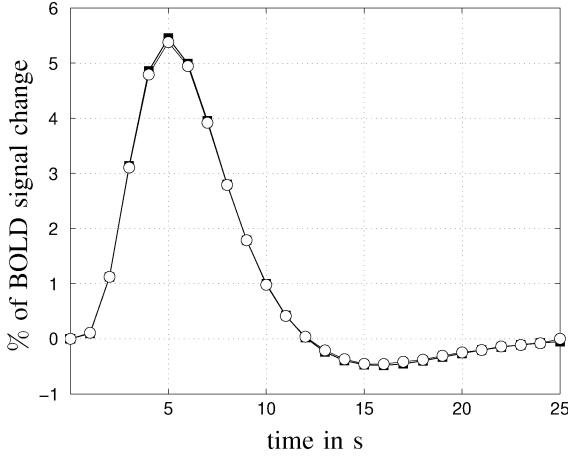


Fig. 2. Symbols \blacksquare and \circ represent the true \mathbf{h}_c and the corresponding HRF estimate, respectively.

the two conditions, we chose the following distributions for the NRLs:

$$\begin{aligned} \mathbf{a}_{j \in C_{1,1}}^1 &\sim \mathcal{N}(\mu_{1,1} = 10, \sigma_{1,1}^2 = 3) \\ \mathbf{a}_{j \in C_{0,1}}^1 &\sim \mathcal{N}(0, \sigma_{0,1}^2 = 1) \\ \mathbf{a}_{j \in C_{1,2}}^2 &\sim \mathcal{N}(\mu_{1,2} = 2, \sigma_{1,2}^2 = 0.3) \\ \mathbf{a}_{j \in C_{0,2}}^2 &\sim \mathcal{N}(0, \sigma_{0,2}^2 = 0.4) \end{aligned}$$

For Condition 1, there were $J_{1,m} = 24$ activated voxels and $J_{0,m} = 38$ nonactivated ones. For condition 2, there were as many as activated voxels as nonactivated ones ($J_{0,m} = J_{1,m} = 30$). For all voxels, the binary stimulus sequence was convolved with the canonical HRF \mathbf{h}_c ,¹ whose exact shape appears in Fig. 2 as the \blacksquare -line. A white Gaussian noise \mathbf{b}_j was then added to the stimulus-induced signal $\sum_m \mathbf{a}_j^m \mathbf{X}^m \mathbf{h}$ in every voxel V_j . The noise variances $(\epsilon_j^2)_{j=1:J}$ were set as follows. Let us introduce the definition of space-varying contrast-to-noise ratio (CNR), based on the L_1 -norm of the signal:

$$\text{CNR}_j \triangleq \frac{\sum_{d,m} |a_j^m h_{d\Delta t}|}{(D-1)\epsilon_j}$$

We restricted our simulations to constant CNR_j in space: $\text{CNR}_j = \text{CNR}, \forall j$. Since the NRLs were sampled from a target distribution (e.g., $p(\mathbf{a}_{j \in C_{i,m}}^m)$ for condition m and class i), the signal norm was different from one voxel to another. To achieve constant CNR, we adapted the noise variances ϵ_j accordingly. Two values of CNR were investigated (CNR = 1.3 and CNR = 0.3), leading first to a simpler synthetic case and, second, to a more realistic one.

Space-varying low-frequency drifts $\mathbf{P}\ell_j$ were added to the fMRI time courses. They were generated from a cosine transform basis whose coefficients ℓ_j were drawn from a normal distribution. The amount of low-frequency signal was tuned to be significant: We checked that the ratio between the quadratic norm of the drift components $\mathbf{P}\ell_j$ and the quadratic norm of the drift-free data $\sum_m \mathbf{a}_j^m \mathbf{X}^m \mathbf{h} + \mathbf{b}_j$ was no less than 50%. The trials of the two conditions were well distributed over time such that collinearity with the low-frequency signal is unlikely.

¹used in the SPM2 software www.fil.ion.ucl.ac.uk/spm/spm2.html

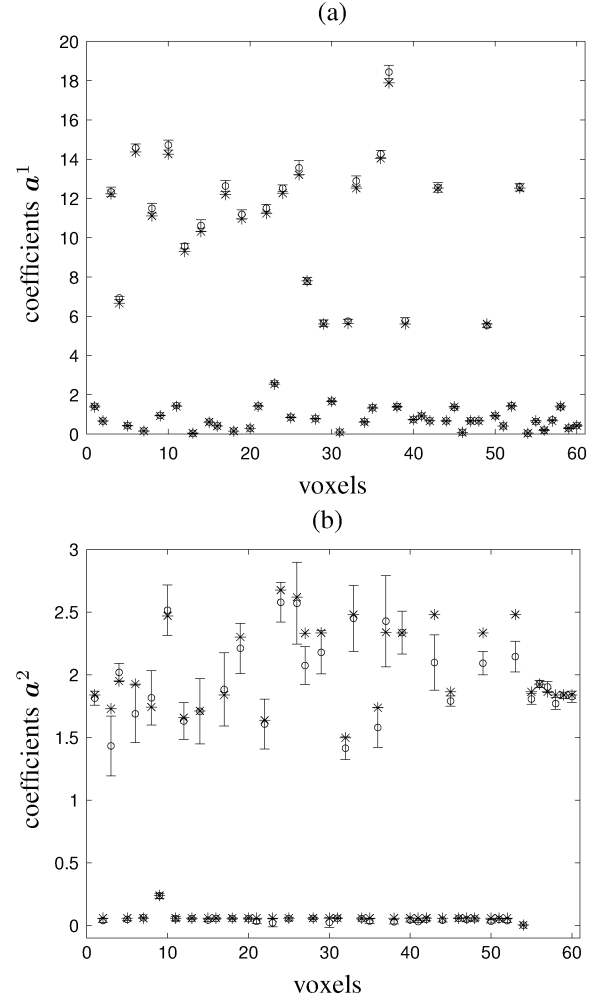


Fig. 3. (a) and (b) provide the NRLs for the first ($m = 1$) and second ($m = 2$) conditions, respectively. Symbols $*$ and \circ represent true and estimated NRLs, respectively. The error bars are derived from the sampled posterior variances given by (5).

The chosen cut-off period (COP) related to the drift term was 70 s. corresponding to $Q = 4$. Synthetic data were then obtained after undersampling the sequences at a $[\text{TR}/\delta t]$ rate, the inter-scan interval being $\text{TR} = 2$ s.

Akin to [28], the sampling rate of the HRF estimate was set to $\Delta t = \delta t$ to avoid estimation bias due to instant-matching error.

B. High CNR (CNR = 1.3)

As shown in Fig. 2, the HRF estimate matches the canonical time course \mathbf{h}_c very well.

Fig. 3(a) and (b) shows the NRL estimates for both conditions. Since the simulated average activity is stronger for $m = 1$ ($\mu_{1,1} = 10$), Fig. 3(a) demonstrates that the response magnitudes of activated voxels are estimated accurately. Indeed, the error bars v_j^m attached to the estimated NRLs and computed as the sampled variances of the NRLs

$$\begin{aligned} v_j^m &= \frac{1}{K_1} \sum_{k=I}^{K_0} \left((a_j^m)^k - \bar{a}_j^m \right)^2 \quad \forall j, m, \text{ with} \\ \bar{a}_j^m &= \frac{1}{K_1} \sum_{k=I}^{K_0} (a_j^m)^k \end{aligned} \quad (5)$$

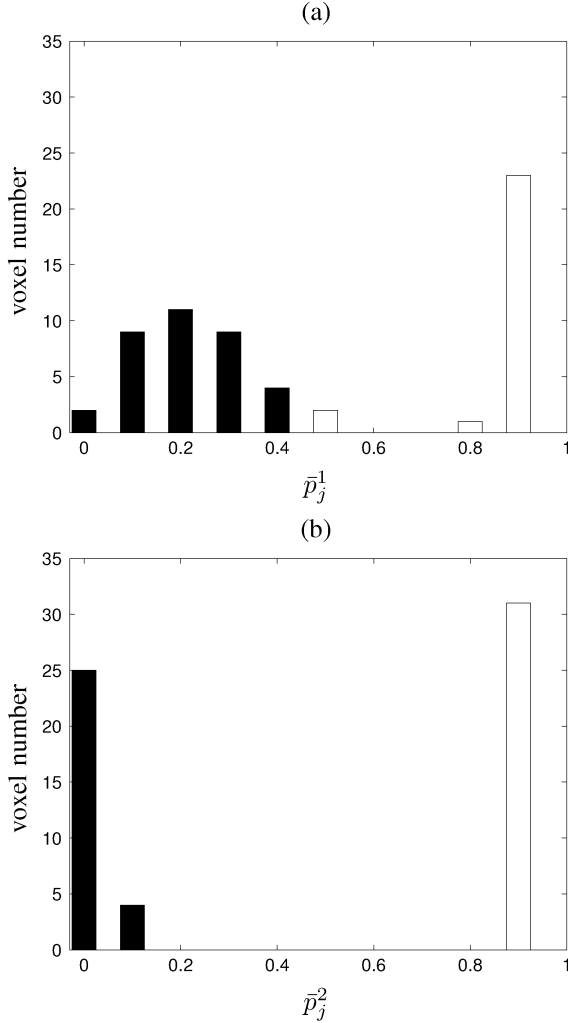


Fig. 4. (a) and (b) describe the histograms of activation probabilities \bar{p}_j^m for $m = 1, 2$, respectively. Filled bars represent nonactivated voxels belonging to $C_{0,m}$ ($\bar{p}_j^m < 0.5$), whereas white bars represent activated voxels (i.e., belonging to $C_{1,m}$).

are small enough to embed the true magnitudes depicted in (*). In contrast, Fig. 3(b) illustrates the influence of a lower mean activity ($\mu_{1,2} = 2$) both on the estimated NRLs and on the corresponding error bars: A small amount of bias, as well as larger sampled variances v_j^m , are observed because of a lower CNR for the second condition. On the other hand, our method behaves normally for nonactivated voxels since estimated and true NRLs overlap.

Fig. 4 shows histograms of activation probabilities \bar{p}_j^m that are computed by averaging the labels q_j^m over iterations

$$\bar{p}_j^m = \frac{1}{K_1} \sum_{k=1}^{K_0} (q_j^m)^k, \quad \forall j, m. \quad (6)$$

Each bar depicted in Fig. 4(a) and (b) returns the number of voxels corresponding to a given value of \bar{p}_j^1 and \bar{p}_j^2 , respectively. Filled bars show nonactivated voxels (i.e., belonging to $C_{0,m}$ because of $(\hat{q}_j^m)^{PM} = 0$) for which $\bar{p}_j^m < 0.5$, whereas white bars represent activated voxels belonging to $C_{1,m}$.

As expected, the histogram depicted in Fig. 4(a) for nonactivated voxels spreads over the left part of the probability axis

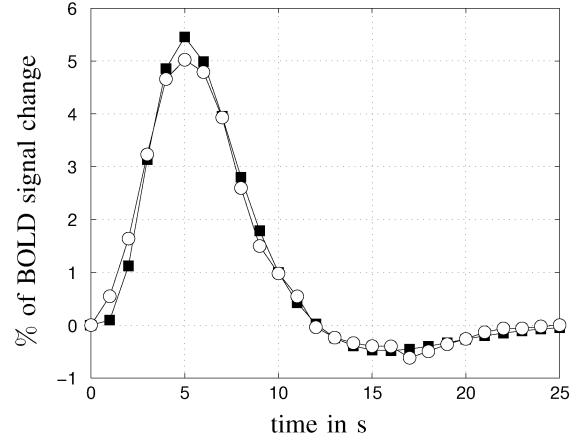


Fig. 5. Symbols \blacksquare and \circ represent true h_c and estimated HRF h , respectively.

because of $\sigma_{0,1}^2 = 1$. The middle part of this graph shows that $\bar{p}_j^1 = 0.5$ for two voxels, indicating that our algorithm hesitates to classify these voxels in class $C_{0,1}$. The right part of the histogram demonstrates that 24 voxels have been assigned to class $C_{1,1}$, as expected. Fig. 4(b) corresponds to an easier case where activated and nonactivated voxels for the second condition are clearly separated and well classified (30 voxels within each class). This results from our variance choice $\sigma_{0,2}^2 = 0.4$.

C. Low CNR (CNR = 0.3)

The HRF estimate plotted in Fig. 5 is a slightly oversmoothed version of h_c about its peak because of the regularization constraint.

Fig. 6(a) and (b) shows the NRL estimates for both conditions. For activated voxels, the estimated magnitudes are more biased for lower CNR. The noise level also has an influence on the confidence intervals, which appear broader for both conditions but, more significantly, for the second one. In contrast, the results for nonactivated voxels show no significant difference in comparison with the first simulation.

Fig. 7 shows histograms of activation probabilities for both conditions. It appears that lower CNR values induce detection of false positives for condition 1, whereas we found 30 voxels in both classes for condition 2. As expected, the number of misclassified voxels is larger for the first condition because of $\sigma_{0,1}^2 = 1$. In Fig. 7(b), it appears that the distribution of nonactivated voxels has a broader dispersion for this CNR in comparison with the first simulation.

VII. RESULTS ON REAL fMRI DATA

A. MRI Parameters

The experiment was performed on a 3-T whole-body system (Bruker, Germany) equipped with a quadrature birdcage radio frequency (RF) coil and a head-gradient coil insert designed for echoplanar imaging. Functional images were obtained with a T2*-weighted gradient echo, echo planar imaging sequence (TR = 2.4 s, TE = 30 ms). A 3-D volume is composed of $64 \times 64 \times 32$ voxels. A high-resolution ($1 \times 1 \times 1.2$ mm) anatomical image using a 3-D gradient-echo inversion-recovery sequence was also acquired for each subject.

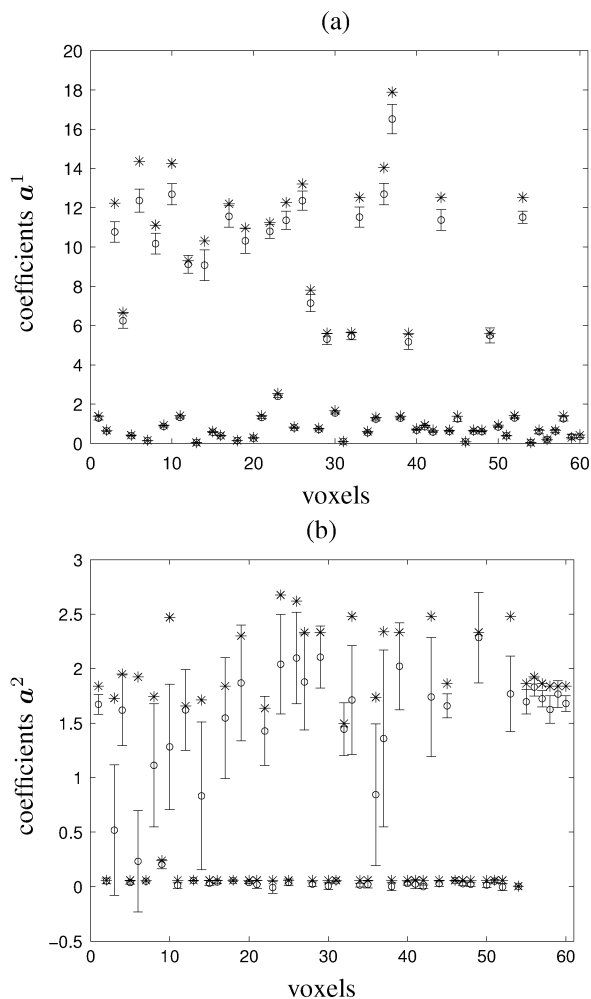


Fig. 6. (a) and (b) provide the NRLs for the first ($m = 1$) and second ($m = 2$) conditions, respectively. Symbols * and o represent true and estimated NRLs, respectively. The error bars are derived from the sampled posterior variances from (5).

B. Experimental Paradigm

The experiment is a fast event-related paradigm. It consisted of a single session of 125 trials ($N = 125$) lasting TR = 2.4 sec each. The main goal of this experiment was to quickly map several brain functions such as motor, visual, and auditory responses, as well as higher cognitive functions like computation, but here, we will focus only on four stimuli: right-hand button click, left-hand button click, audio, and video.

The chosen ROIs are SPM clusters obtained from t maps (thresholded at $P = 0.001$ corrected for multiple comparisons) based on standard SPM activation detection using a canonical model, least squares estimation, and inference on relevant contrasts.

In the following, we choose to study two contrasts: (right click minus left click) contrast and (audio minus video) contrast. ROIs \mathcal{R}_1 and \mathcal{R}_2 were defined using the MARSBAR toolbox.² The 178 voxels of the (right click minus left click) \mathcal{R}_1 are located around the voxel of Talairach coordinates in millimeters: ($X = -36, Y = -21, Z = 48$). The 632 voxels of the (audio minus video) \mathcal{R}_2 are located around the voxel of Talairach coordinates in millimeters: ($X = -63, Y = -21, Z = 3$).

²www.sourceforge.net/projects/marsbar

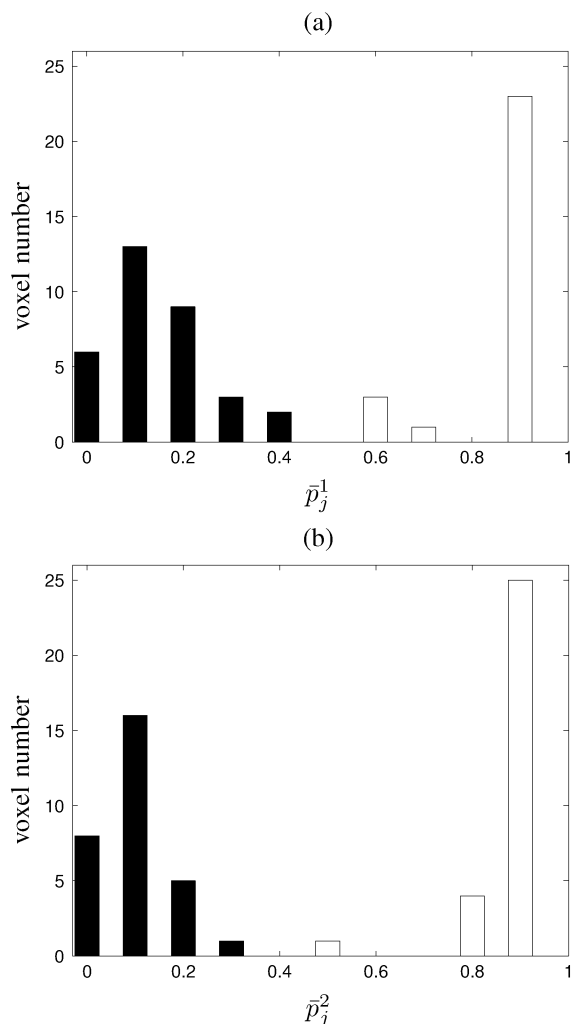


Fig. 7. (a) and (b) describe the histograms of activation probability \bar{p}_j^m for $m = 1, 2$, respectively. Filled bars represent nonactivated voxels belonging to $C_{0,m}(\bar{p}_j^m < 0.5)$, whereas white bars represent activated voxels (i.e., belonging to $C_{1,m}$).

C. Results

In Figs. 8(a) and 9(a), the HRF estimates corresponding to the two selected ROIs (\mathcal{R}_1 and \mathcal{R}_2) are plotted. These HRF estimates have a regular shape, as enforced by the prior model. Figs. 8(b)–(c) and 9(b)–(c) show the maps of the NRL estimates computed for the right and left clicks in \mathcal{R}_1 and for the audio and video conditions in \mathcal{R}_2 , respectively. Note the different scaling in these figures, and as expected, high values are found for the right click condition in \mathcal{R}_1 defined with a (right click minus left click) contrast, whereas positive or negative values close to 0 are found for the left click. The same apply for the (audio minus video) contrast.

Figs. 8(d)–(e) and 9(d)–(e) show the voxels classification in class 0 (red) and in class 1 (white). Classification was based on the maximum likelihood principle (e.g., voxels with greater chance to be in class 1 than in class 0 are classified in 1). It is crucial to note that voxels classified in class 1 [for instance, for the left click in Fig. 8(c)] are not necessarily “activated” in the usual sense used in neuroimaging results but can only be said to be more likely in class 1. Whether they are “activated” depends on whether class 1 can be differentiated from class 0. Indeed, as shown in

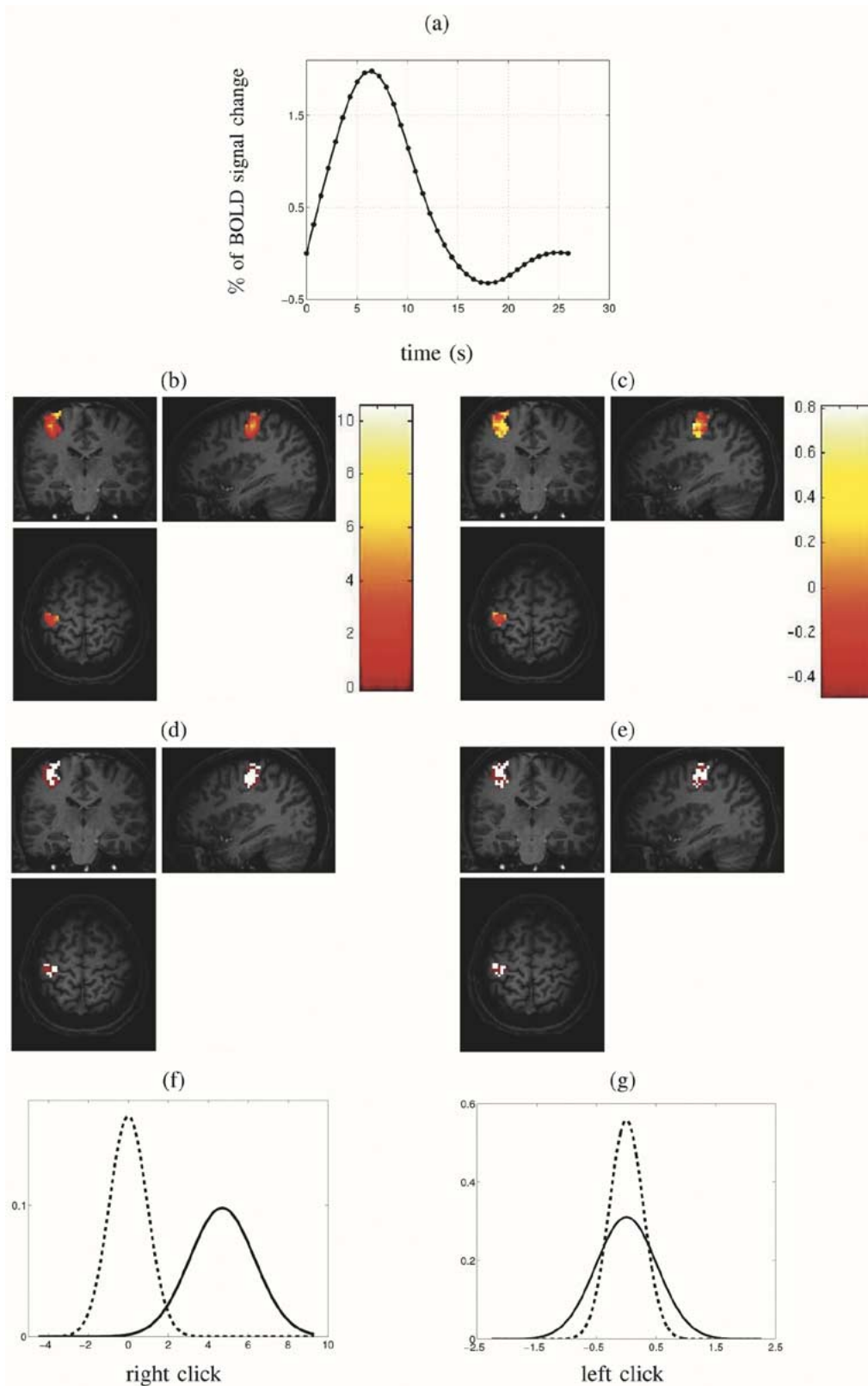


Fig. 8. Estimation results for the (right click minus left click) contrast using raw (unsmoothed) data. From top to bottom and from left to right. (a) HRF estimate for \mathcal{R}_1 defined from the (right click minus left click) contrast. (b) Right click voxels NRLs estimates. (c) Left click voxels NRLs estimates. (d) and (e) Classification results for the right and left click stimulus, respectively (red: class 0, white: class 1). (f) and (g) Classes distributions of the right and left click stimuli, respectively. Dashed lines: class 0. Solid lines: class 1. Values are only plotted for voxels in the chosen ROI and not for all voxels in the brain.

Fig. 8(f)–(g), the estimated distributions of the two classes may be too close to each other to make their discrimination from the neural response levels efficient. To cope with this issue, we have

implemented a classical test of the null hypothesis to keep voxels that survive a 5% risk of false positive threshold, as illustrated in Fig. 9(f)–(g). Clearly, the region of interest is almost entirely sig-

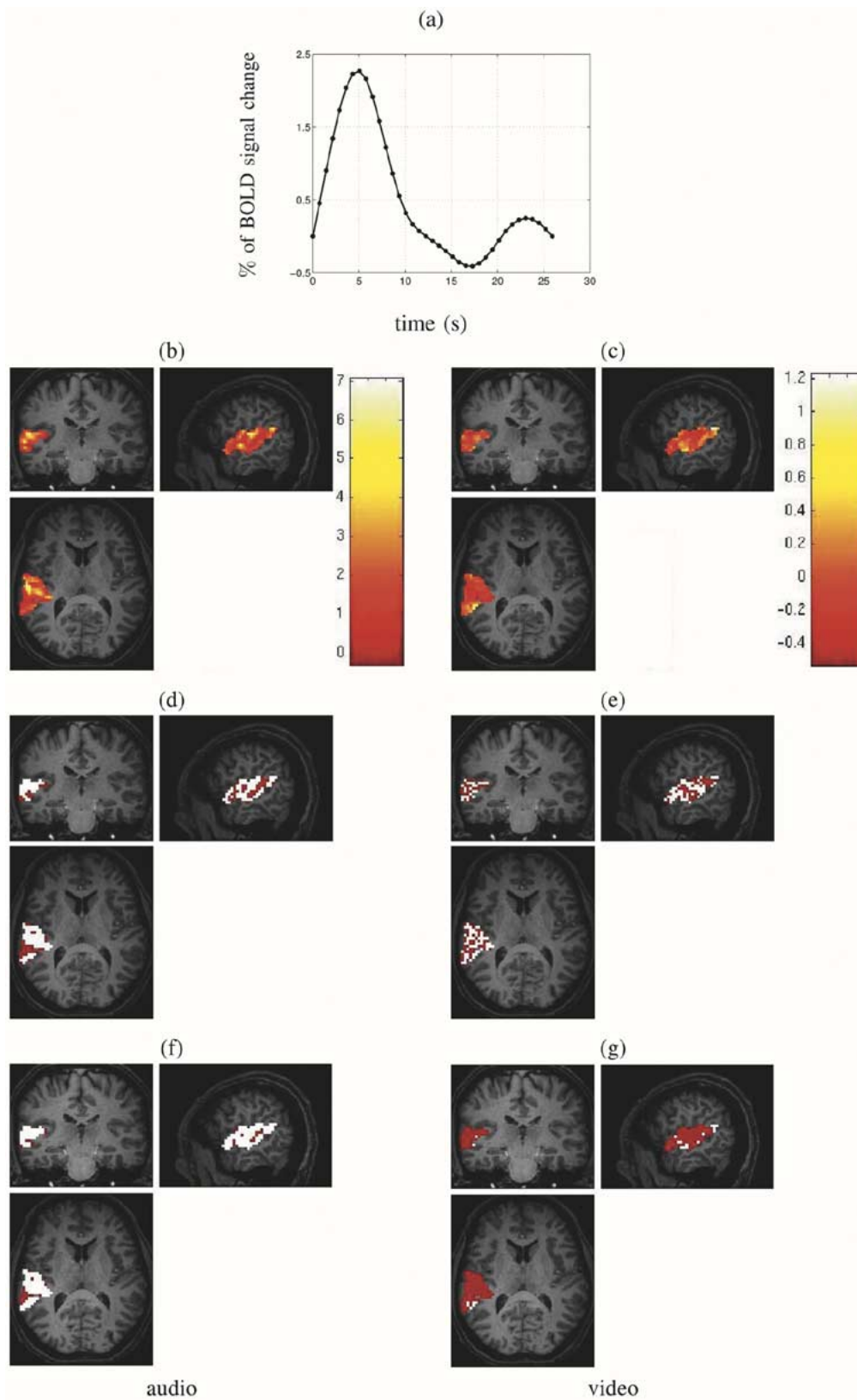


Fig. 9. Estimation results for the (audio minus video) contrast using raw (unsmoothed) data. From top to bottom and from left to right. (a) HRF estimate for \mathcal{R}_2 defined from the (audio minus video) contrast. (b) and (c) Audio (resp. video) voxels NRLs estimates. (d) and (e) Classification results for the audio and video stimulus, respectively (red: class 0, white: class 1). (f) and (g) Statistical test results for the audio (resp. video) stimulus after at the 5% risk of error. Significantly activated voxels are in white, and nonsignificant voxels are in red. Values are only plotted for voxels in the ROI and not for all voxels in the brain.

nificantly activated for the audio condition, whereas few voxels survive this threshold for the video condition.

Our approach was also tested using data smoothed with a 6-mm isotropic Gaussian kernel. Essential results conveyed the

same information, with a greater spatial homogeneity observed in all results (voxels NRL activity, voxels classifications, significant voxels). Results are not reported here but are available from the authors.

The *a priori* classification in two classes may seem as a constraint. Since no formal model testing is performed to choose between a model including only one class with the model that includes two classes, the interpretation of the data classified in class 1 is not straightforward when, for a given condition, the ROI is actually made up of nonactivated voxels. In this case, a model with only one class would be more suitable. However, we showed that a simple hypothesis testing procedure can be used for the detection of “activated” voxels. Besides, the implementation of a Bayesian information criterion would also easily raise this limitation. Note also that a threshold corrected for multiple comparison can be used if a strong specificity is needed from the analysis. In our experimental results, classes 1 and 0 were straightforwardly close or different because of our ROI choice. This may not be the case in other experimental conditions or if ROIs are selected on an anatomical basis.

The knowledge of the alternative hypothesis estimation (class 1 estimated model) is information that is to date not normally used in neuroimaging analyses but allows one to ask some different classes of questions to the data that cannot be answered in the null hypothesis testing framework. For instance, one may ask whether a given voxel activity is indeed not activated (its value is close to zero within a given confidence interval); this is information that is not obtainable from the “nonrejection” of the null hypothesis. Furthermore, one would also be able to control for the risk of false *negative* by setting a threshold based on the alternative distribution.

VIII. CONCLUSION

In this paper, we have proposed an original method for semi-blind deconvolution of impulse pseudo-neural response in functional neuroimaging. This method extends a previous work [28] to deal with regional HRF estimation in an efficient way while modeling the spatial variability of the pseudo-neural response for each stimulus type. Mixture modeling provides us a way of estimating the distributions of activated and nonactivated voxels from the data itself. Indeed, detection is performed on the estimated class 0 (centered on 0) and class 1 distribution parameters. To our knowledge, it is the first time that a Bayesian joint detection-estimation approach is proposed for the analysis of fMRI data. We have validated this approach on both synthetic and real fMRI data. The method is general enough to deal with all specific features of fMRI data (several sessions per subject, voxel specific noise variance, asynchronous timing between event onsets and scanning time, physiological artifacts, and so on). Our optimization scheme is also efficient enough to allow for large fMRI time series to be processed. Furthermore, this approach provides a tool to compare estimated activity between conditions, regions, or subjects.

Compared with standard detection techniques (like SPM), this paper introduces the joint estimation of the shape of the HRF and the associated spatial map and, therefore, should yield more precise estimations of voxel activity. Our modeling also

permits the use of the estimated distribution of activity under the “alternative” hypothesis in a Bayesian framework. In this regard, this approach provides the neuroscientist with a method that is able to answer questions that are not tractable in the classical null hypothesis framework [21]. Another advantage of estimating the “alternative” distribution is that it allows some adjustment for modeling assumption violations. In the case of imperfect modeling of the noise characteristics, for instance, the null distribution may have a different form from what is currently assumed in the null-hypothesis testing framework [21]. However, mixture modeling-based approaches may fail when the data does not meet the distributional assumptions, whatever the source of discrepancy (non Gaussianity, three-class mixture model, . . .). This point is critical in our approach for stimulus types that do not elicit activation in any voxel of the selected ROI. This could be solved using a model selection step that requires the estimation of the parameters of the simpler one-class model described in [32].

The method can be extended in several ways. First, spatial regularization could be introduced on the spatial map of classification labels using 2-D (based on the cortical surface) or three-dimensional (3-D) (based on the volume) Markov random fields. The specific use of Pickard random fields could be particularly interesting to automatically tune the amount of regularization from the data without facing the estimation of the *partition function* [56]. Another solution has been recently proposed to cope with the same issue [47].

Second, the model presented here assumes that the NRLs are constant in time. However, phenomena such as adaptation or learning may be better modeled by including the time dimension in more sophisticated models. This is the subject of future research. Third, anatomical information (grey/white matter) have yet to be considered. However, we know that activation should be localized in the grey matter of the brain, and sophisticated segmentation tools of anatomical data are now available (see, for instance, the Brainvisa software³). If good registration between the anatomical and functional data can be achieved, this information should be taken into account in the model formulation as a prior.

Last, white noise is assumed in this paper. We have started to develop an extension that accounts for serial correlation of fMRI time series using a spatially varying first-order AR model of errors [41]. First, this extension is more computationally demanding since AR, as well as drift parameters, now need to be sampled. Our first tests on simulations have shown that this modeling has an influence over the posterior error bars of the NRLs. More precisely, for correlated synthetic datasets, we get smaller error bars when modeling this correlation. Nonetheless, our first tests on real fMRI data yielded no major improvement compared with the results described in Section VII.

APPENDIX

A. Computational Details

We will use specific notations to make reference to usual distributions (see Table III). In the following, we derive the poste-

³<http://brainvisa.info/index.html>

TABLE III
LIST OF DISTRIBUTION NOTATIONS

\mathcal{U}	uniform distribution
\mathcal{N}	Gaussian distribution
\mathcal{IG}	Inverse Gamma distribution
\mathcal{B}	Beta distribution

rrior full conditional distributions from which we sample in our algorithm.

1) *Hemodynamic Response Function*: The full conditional posterior pdf $p(\mathbf{h} | \mathbf{y}, \mathbf{a}, \Theta)$ can be identified from the full posterior pdf $p(\mathbf{h}, \mathbf{a}, \Theta | \mathbf{y})$, assuming that $(\mathbf{a}, \Theta, \mathbf{y})$ are constant, while \mathbf{h} may still vary: $p(\mathbf{h} | \mathbf{y}, \mathbf{a}, \Theta) \propto p(\mathbf{y} | \mathbf{h}, \mathbf{a}, \epsilon^2) p(\mathbf{h})$. Since the likelihood and the prior are Gaussian, \mathbf{h} also follows a Gaussian conditional distribution $p(\mathbf{h} | \text{rest}) \sim \mathcal{N}(\mathbf{m}_h, \Sigma_h)$, with

$$\begin{aligned} \Sigma_h^{-1} &= \sigma_h^{-2} \mathbf{R}^{-1} + \sum_j \mathbf{S}_j^t \mathbf{Q}_j \mathbf{S}_j, \\ \mathbf{m}_h &= \Sigma_h \sum_j \mathbf{S}_j^t \mathbf{Q}_j \mathbf{y}_j \end{aligned} \quad (7)$$

where $\mathbf{S}_j = \sum_m a_j^m \mathbf{X}^m$. In practice, drawing realizations from $p(\mathbf{h} | \text{rest})$ is a three-step procedure [51].

- 1) Compute the square root of matrix Σ_h . This can be achieved using Cholesky factorization such that $\Sigma_h = \mathbf{L}\mathbf{L}^t$, where \mathbf{L} is a lower triangular matrix.
- 2) Generate a Gaussian vector $\mathbf{k} \sim \mathcal{N}(\mathbf{0}, \mathbf{I}_{D-1})$.
- 3) Compute $\mathbf{h} = \mathbf{m}_h + \mathbf{L}\mathbf{k}$ to get a sample from $\mathcal{N}(\mathbf{m}_h, \Sigma_h)$.

2) *HRF Scale*: Sampling the hyperparameter σ_h^2 amounts to simulating according to

$$p(\sigma_h^2 | \text{rest}) = p(\sigma_h^2 | \mathbf{h}) \sim \mathcal{IG}(D/2, \mathbf{h}^t \mathbf{R}^{-1} \mathbf{h} / 2). \quad (8)$$

3) *“Neural” Response Levels*: The sampling scheme of the NRLs relies on two nested loops, where the inner corresponds to the stimulus types (e.g., index m) and the outer to voxels (e.g., index j). The basic operation is to sample each a_j^m from the conditional distribution

$$p(a_j^m | \text{rest}) = p(a_j^m | \mathbf{y}_j, \mathbf{h}, \theta_m, \epsilon_j^2, z_j^{m' \neq m}).$$

This pdf is the marginal distribution of an *a posteriori* Gaussian mixture:

$$\begin{aligned} & p(a_j^m | \mathbf{y}_j, \mathbf{h}, \theta_m, \epsilon_j^2, z_j^{m' \neq m}) \\ &= \sum_{i=0,1} p(a_j^m | q_j^m = i, \mathbf{y}_j, \mathbf{h}, \epsilon_j^2, z_j^{m' \neq m}) \Pr(q_j^m = i) \\ &\sim \sum_{i=0,1} \lambda_{i,j}^m \mathcal{N}(\mu_{i,j}^m, (\sigma_{i,j}^m)^2). \end{aligned} \quad (9)$$

After some straightforward calculations, we get the expression of the mixture parameters

$$\begin{aligned} (\sigma_{i,j}^m)^{-2} &= \sigma_{i,m}^{-2} + \mathbf{g}_m^t \mathbf{Q}_j \mathbf{g}_m, \\ \mu_{i,j}^m &= (\sigma_{i,j}^m)^{-2} (\mathbf{g}_m^t \mathbf{Q}_j \mathbf{e}_{m,j} + i \mu_{i,m} \sigma_{i,m}^{-2}) \end{aligned}$$

where $\mathbf{g}_m = \mathbf{X}^m \mathbf{h}$, and $\mathbf{e}_{m,j} = \mathbf{y}_j - \sum_{m' \neq m} a_j^{m'} \mathbf{g}_{m'} = \tilde{\mathbf{y}}_j + a_j^m \mathbf{g}_m$. The weighting probability $\lambda_{i,j}^m$ of the two distributions can be expressed as follows:

$$\begin{aligned} \lambda_{i,j}^m &= \left(1 + \tilde{\lambda}_{1-i,j}^m / \tilde{\lambda}_{i,j}^m\right)^{-1} \\ \tilde{\lambda}_{i,j}^m &= \frac{\lambda_{i,m}^2 \lambda_{1-i,m} \sigma_{i,j}^m}{\sigma_{i,m}} \\ &\times \exp\left(\left(\mu_{i,j}^m\right)^2 / 2 \left(\sigma_{i,j}^m\right)^2\right), \quad i = 0, 1. \end{aligned}$$

As indicated in (9), we first need to sample the binary label q_j^m . For doing so, we generate u_j^m from $\mathcal{U}([0, 1])$, and the following rule applies:

$$u_j^m \leq \lambda_{1,j}^m \implies q_j^m = 1, \quad \text{otherwise } q_j^m = 0.$$

Then, the sampling of the NRL a_j^m is based on the full conditional pdf $p(a_j^m | q_j^m = i, \mathbf{y}_j, \mathbf{h}, \epsilon_j^2, z_j^{m' \neq m})$:

$$p(a_j^m | q_j^m = i, \mathbf{y}_j, \mathbf{h}, \theta_m, \epsilon_j^2) \sim \mathcal{N}(\mu_{i,j}^m, (\sigma_{i,j}^m)^2), \quad i = 0, 1. \quad (10)$$

4) *Noise Variances*: Sampling the noise variances σ_ϵ^2 can be performed in parallel. Let us denote $\mathbf{a}_j = (a_j^m)_{m=1:M}$. Then, drawing a sample from $p(\sigma_\epsilon^2 | \text{rest})$ is straightforward, according to

$$\begin{aligned} p(\epsilon_j^2 | \text{rest}) &= p(\epsilon_j^2 | \mathbf{y}_j, \mathbf{h}, \mathbf{a}_j) \propto p(\mathbf{y}_j | \mathbf{h}, \mathbf{a}_j, \epsilon_j^2) \\ &\sim \mathcal{IG}\left((N+1-Q)/2, \|\tilde{\mathbf{y}}_j\|_{\mathbf{I}_N - \mathbf{P}\mathbf{P}^t}^2 / 2\right) \end{aligned} \quad (11)$$

5) *Weighting Probabilities*: Sampling the weighting probabilities λ can be parallelized as well since λ_m is independent of $m' \neq m$. For simplicity, drawing a realization of λ_m consists of sampling from a Beta distribution

$$\begin{aligned} p(\lambda_m | \text{rest}) &= p(\lambda_m | \mathbf{q}^m) \propto p(\mathbf{q}^m | \lambda_m) p(\lambda_m) \\ &\sim \mathcal{B}(J_{1,m} + 3/2, J_{0,m} + 3/2) \end{aligned} \quad (12)$$

where $\mathbf{q}^m = (q_j^m)_{j=1:J}$. $J_{i,m}$ stands for the number of voxels in class $C_{i,m}$ for condition m . Note that $J_{1-i,m} = J - J_{i,m}$ for $i = 0, 1$.

6) *Mixture Parameters*: Here, we focus on the generation of realizations of hyperparameters $\sigma_{0,m}^2$ and $(\mu_{1,m}, \sigma_{1,m}^2)$ attached to classes $C_{0,m}$ and $C_{1,m}$, respectively:

$$\begin{aligned} p(\sigma_{0,m}^2 | \text{rest}) &= p(\sigma_{0,m}^2 | \mathbf{z}^m) \\ p(\mu_{1,m}, \sigma_{1,m}^2 | \text{rest}) &= p(\mu_{1,m}, \sigma_{1,m}^2 | \mathbf{z}^m) \end{aligned}$$

where $\mathbf{z}^m = (\mathbf{a}^m, \mathbf{q}^m)$. Note that both the labels \mathbf{q}^m and the corresponding NRLs \mathbf{a}^m have to be known to be sampled from

the right posterior distribution for condition m . Bayes' rule enables us to derive the closed-form expression of these pdfs:

$$\begin{aligned} & p(\sigma_{0,m}^2 | \mathbf{z}^m) \\ & \propto p(\mathbf{a}^m | \mathbf{q}^m, \mathbf{y}, \sigma_{0,m}^2) \Pr(\mathbf{q}^m) p(\sigma_{0,m}^2) \\ & \propto \sigma_{0,m}^{-1} \prod_{j \in C_{0,m}} p(a_j^m | q_j^m = 0, \mathbf{y}, \sigma_{0,m}^2) \\ & p(\mu_{1,m}, \sigma_{1,m}^2 | \mathbf{z}^m) \\ & \propto p(\mathbf{a}^m | \mathbf{q}^m, \mathbf{y}, \mu_{1,m}, \sigma_{1,m}^2) \Pr(\mathbf{q}^m) p(\mu_{1,m}, \sigma_{1,m}^2) \\ & \propto \sigma_{1,m}^{-1} \prod_{j \in C_{1,m}} p(a_j^m | q_j^m = 1, \mathbf{y}, \mu_{1,m}, \sigma_{1,m}^2). \end{aligned}$$

For $i = 0, 1$, let

$$\begin{aligned} \nu_{i,m} &= \sum_{j \in C_{i,m}} (a_j^m - \eta_{i,m})^2 \quad \text{and} \\ \eta_{i,m} &= \frac{1}{J_{i,m}} \sum_{j \in C_{i,m}} a_j^m. \end{aligned}$$

According to (10), $\{a_j^m\}_{j \in C_{0,m}}$ are i.i.d. variables, each being distributed according to $\mathcal{N}(0, \sigma_{0,m}^2)$ -distributed. The ensuing posterior pdf of $\sigma_{0,m}^2$ therefore reads

$$(\sigma_{0,m}^2 | \mathbf{z}^m) \sim \mathcal{IG}\left(\frac{J_{0,m} - 1}{2}, \frac{\nu_{0,m}}{2}\right). \quad (13)$$

For class $C_{1,m}$, we need to sample from the joint pdf of $(\mu_{1,m}, \sigma_{1,m}^2)$. This can be decomposed in two steps using ([51, Prop. 4.4.1, p 187]).

- 1) Draw a sample for the variance from $p(\sigma_{1,m}^2 | \mathbf{z}^m)$

$$(\sigma_{1,m}^2 | \mathbf{z}^m) \sim \mathcal{IG}\left(\frac{J_{1,m} - 1}{2}, \frac{\nu_{1,m}}{2}\right). \quad (14)$$

- 2) Draw a sample for the mean from the conditional posterior pdf

$$p(\mu_{1,m} | \sigma_{1,m}^2, \mathbf{z}^m) \sim \mathcal{N}\left(\eta_{1,m}, \frac{\sigma_{1,m}^2}{J_{1,m}}\right). \quad (15)$$

ACKNOWLEDGMENT

The authors are grateful to the anonymous reviewers for their valuable comments.

REFERENCES

- [1] S. Ogawa, T. Lee, A. Kay, and D. Tank, "Brain magnetic resonance imaging with contrast dependent on blood oxygenation," *Proc. Nat. Acad. Sci. USA*, vol. 87, no. 24, pp. 9868–9872, 1990.
- [2] C. Goutte, P. Toft, E. Rostrup, F. A. Nielsen, and L. K. Hansen, "On clustering fMRI time series," *Neuroimag.*, vol. 9, no. 3, pp. 298–310, 1999.
- [3] M. Fadili, S. Ruan, D. Bloyet, and B. Mazoyer, "A multistep unsupervised fuzzy clustering analysis of fMRI time series," *Hum. Brain Mapp.*, vol. 10, no. 4, pp. 160–178, 2000.
- [4] R. Baumgartner, L. Ryner, W. Richter, R. Summers, M. Jarmasz, and R. Somorjai, "Comparison of two exploratory data analysis methods for fMRI: Fuzzy clustering vs. principal component analysis," *Magn. Reson. Imaging*, vol. 18, no. 1, pp. 89–94, 2000.

- [5] A. Anderson, D. Grash, and M. Avison, "Principal component analysis of the dynamic response measured by fMRI: A generalized linear systems framework," *J. Magn. Reson. Imag.*, vol. 17, pp. 795–815, 1999.
- [6] M. McKeown, "Detection of consistently task-related activation in fMRI data with hybrid independent component analysis," *Neuroimag.*, vol. 11, pp. 24–35, 2000.
- [7] V. Calhoun, T. Adali, G. Pearlson, and J. Pekar, "Spatial and temporal independent component analysis of functional MRI data containing a pair of task-related waveforms," *Hum. Brain Mapp.*, vol. 13, pp. 43–53, 2001.
- [8] R. S. J. Frackowiak, K. J. Friston, C. D. Dolan, and J. C. Mazziotta, *Human Brain Function*. New York: Academic, 1997.
- [9] D. Malonek and A. Grinvald, "Interactions between electrical activity and cortical microcirculation revealed by imaging spectroscopy: Implications for functional brain mapping," *Science*, vol. 272, pp. 551–554, 1996.
- [10] R. B. Buxton, E. C. Wong, and L. R. Frank, "Dynamics of blood flow and oxygenation changes during brain activation: The balloon model," *Magn. Reson. Med.*, vol. 39, pp. 855–864, Jun. 1998.
- [11] J. Mandeville, J. Marota, C. Ayata, C. Zaharchuck, M. Moskowitz, B. Rosen, and R. Weisskoff, "Evidence of a cerebro-vascular post-arteriole windkessel with delayed compliance," *J. Cereb. Blood Flow Metab.*, vol. 19, pp. 679–689, 1999.
- [12] K. J. Friston, A. Mechelli, R. Turner, and C. J. Price, "Nonlinear responses in fMRI: the balloon model, Volterra kernels, and other hemodynamics," *Neuroimag.*, vol. 12, pp. 466–477, 2000.
- [13] J. Riera, J. Watanabe, I. Kazuki, M. Naoki, E. Aubert, T. Ozaki, and R. Kawashima, "A state-space model of the hemodynamic approach: Nonlinear filtering of BOLD signal," *Neuroimag.*, vol. 21, pp. 547–567, 2004.
- [14] N. Lange, "Empirical and substantive models, the Bayesian paradigm, and meta-analysis in functional brain imaging," *Hum. Brain Mapp.*, vol. 5, pp. 259–263, 1997.
- [15] M. S. Cohen, "Parametric analysis of MRI data using linear systems methods," *Neuroimag.*, vol. 6, pp. 93–103, 1997.
- [16] J. C. Rajapakse, F. Kruggel, J. M. Maisog, and D. Von Cramon, "Modeling hemodynamic response for analysis of functional MRI time-series," *Hum. Brain Mapp.*, vol. 6, pp. 283–300, 1998.
- [17] G. H. Glover, "Deconvolution of impulse response in event-related BOLD fMRI," *Neuroimag.*, vol. 9, pp. 416–429, 1999.
- [18] G. K. Aguirre, E. Zarahn, and M. D'Esposito, "The variability of human bold hemodynamic responses," *Neuroimag.*, vol. 7, p. 574, 1998.
- [19] R. L. Buckner, J. Goodman, M. Burock, M. Rotte, W. Koutstaal, D. L. Schachter, B. R. Rosen, and A. M. Dale, "Functional-anatomic correlates of object priming in humans revealed by rapid presentation event-related fMRI," *Neuron*, vol. 20, pp. 285–296, 1998.
- [20] F. M. Miezin, L. Maccotta, J. M. Ollinger, S. E. Petersen, and R. L. Buckner, "Characterizing the hemodynamic response: Effects of presentation rate, sampling procedure, and the possibility of ordering brain activity based on relative timing," *Neuroimag.*, vol. 11, pp. 735–759, 2000.
- [21] K. J. Friston, A. P. Holmes, K. Worsley, J.-B. Poline, C. Frith, and R. Frackowiak, "Statistical parametric maps in functional neuroimaging: A general linear approach," *Hum. Brain Mapp.*, vol. 2, pp. 189–210, 1995.
- [22] O. Joseph and R. N. Henson, "Event-related functional magnetic resonance imaging: Modeling, inference and optimization," *Philos. Trans. R. Soc. Lond. B: Biol.*, vol. 354, no. 1387, pp. 1215–1228, 1999.
- [23] C. Genovese, "A Bayesian time-course model for functional magnetic resonance imaging data (with discussion)," *J. Acoust. Soc. Amer.*, vol. 95, pp. 691–719, 2000.
- [24] C. Gössl, L. Fahrmeir, and D. P. Auer, "Bayesian modeling of the hemodynamic response function in BOLD fMRI," *Neuroimag.*, vol. 14, pp. 140–148, 2001.
- [25] M. Woolrich, M. Jenkinson, J. Brady, and S. Smith, "Fully Bayesian spatio-temporal modeling of fMRI data," *IEEE Trans. Med. Imag.*, vol. 23, no. 2, pp. 213–231, Feb. 2004.
- [26] C. Goutte, F. A. Nielsen, and L. K. Hansen, "Modeling the haemodynamic response in fMRI using smooth filters," *IEEE Trans. Med. Imag.*, vol. 19, no. 12, pp. 1188–1201, Dec. 2000.
- [27] G. Marrelec, H. Benali, P. Ciuciu, M. Péligrini-Issac, and J.-B. Poline, "Robust Bayesian estimation of the hemodynamic response function in event-related BOLD MRI using basic physiological information," *Hum. Brain Mapp.*, vol. 19, no. 1, pp. 1–17, 2003.
- [28] P. Ciuciu, J.-B. Poline, G. Marrelec, J. Idier, C. Pallier, and H. Benali, "Unsupervised robust nonparametric estimation of the hemodynamic response function for any fMRI experiment," *IEEE Trans. Med. Imag.*, vol. 22, no. 10, pp. 1235–1251, Oct. 2003.

- [29] P. Ciuciu, J. Idier, A. Roche, and C. Pallier, "Outlier detection for robust region-based estimation of the hemodynamic response function in event-related fMRI," in *Proc. 2th Proc. IEEE ISBI*, Arlington, VA, 2004, pp. 392–395.
- [30] C. Gössl, D. P. Auer, and L. Fahrmeir, "Dynamic models in fMRI," *Magn. Reson. Med.*, vol. 43, pp. 72–81, 2000.
- [31] —, "Bayesian spatio-temporal modeling of the hemodynamic response function in BOLD fMRI," *Biometr.*, vol. 57, pp. 554–562, 2001.
- [32] S. Makni, P. Ciuciu, J. Idier, and J.-B. Poline, "Semi-blind deconvolution of neural impulse response in event-related fMRI using Gibbs sampler," in *Proc. 2th Proc. IEEE ISBI*, Arlington, VA, 2004, pp. 860–863.
- [33] N. V. Hartvig and J. Jensen, "Spatial mixture modeling of fMRI data," *Hum. Brain Mapp.*, vol. 11, no. 4, pp. 233–248, 2000.
- [34] B. S. Everitt and E. T. Bullmore, "Mixture model mapping of brain activation in functional magnetic resonance images," *Hum. Brain Mapp.*, vol. 7, pp. 1–14, 1999.
- [35] G. Marrelec, P. Ciuciu, M. Péligrini-Issac, and H. Benali, "Estimation of the hemodynamic response function in event-related functional MRI: Bayesian networks as a framework for efficient Bayesian modeling and inference," *IEEE Trans. Med. Imag.*, vol. 23, no. 8, pp. 959–967, Aug. 2004.
- [36] E. Zarahn, G. K. Aguirre, and M. D'Esposito, "Empirical analysis of BOLD fMRI statistics. I. Spatially unsmoothed data collected under null-hypothesis conditions," *Neuroimag.*, vol. 5, pp. 179–197, 1997.
- [37] F. G. Meyer, "Wavelet-based estimation of a semi-parametric generalized linear model of fMRI time series," *IEEE Trans. Med. Imag.*, vol. 22, no. 3, pp. 315–322, Mar. 2003.
- [38] E. T. Bullmore, M. Brammer, S. C. Williams, S. Rabe-Hesketh, N. Janot, A. David, J. Mellers, R. Howard, and P. Sham, "Statistical methods of estimation and inference for functional MR image analysis," *Magn. Reson. Med.*, vol. 35, pp. 261–277, 1996.
- [39] M. Woolrich, B. Ripley, M. Brady, and S. Smith, "Temporal autocorrelation in univariate linear modeling of fMRI data," *Neuroimag.*, vol. 14, no. 6, pp. 1370–1386, 2001.
- [40] K. Worsley, C. Liao, J. Aston, V. Petre, G. Duncan, F. Morales, and A. Evans, "A general statistical analysis for fMRI data," *Neuroimag.*, vol. 15, no. 1, pp. 1–15, 2002.
- [41] S. Makni, P. Ciuciu, J. Idier, and J.-B. Poline, (2005) Joint Detection-Estimation of Brain Activity in fMRI: An Extended Model Accounting for Serial Correlation. CEA/SHFJ, Orsay, France. [Online]. Available: <http://www.madic.org/biblio/en/Year/2005.php>
- [42] G. Marrelec, H. Benali, P. Ciuciu, and J.-B. Poline, "Bayesian estimation of the hemodynamic response function in functional MRI," in *Proc. Bayesian Inference Maximum Entropy Methods Workshop*, R. Fry, Ed., 2001.
- [43] G. Flandin, F. Kherif, X. Pennec, D. Rivière, N. Ayache, and J.-B. Poline, "Parcellation of brain images with anatomical and functional constraints for fMRI data analysis," in *Proc. First Proc. IEEE ISBI*, Washington, DC, 2002, pp. 907–910.
- [44] B. Thirion and O. Faugeras, "Feature detection in fMRI data: The information bottleneck approach," in *Proc. 6th MICCAI*, Montréal, QC, Canada, 2003, pp. 83–91.
- [45] W. Penny, N. Trujillo-Barreto, and K. J. Friston, "Bayesian fMRI time series analysis with spatial priors," *Neuroimag.*, vol. 23, no. 2, pp. 350–362, 2005.
- [46] M. Smith, B. Pütz, D. Auer, and L. Fahrmeir, "Assessing brain activity through spatial Bayesian variable selection," *Neuroimag.*, vol. 20, pp. 802–815, 2003.
- [47] M. Woolrich, T. Behrens, C. Beckmann, and S. Smith, "Mixture models with adaptive spatial regularization for segmentation with an application to fMRI data," *IEEE Trans. Med. Imag.*, vol. 24, no. 1, pp. 1–11, Jan. 2005.
- [48] Q. Cheng, R. Chen, and T.-H. Li, "Simultaneous wavelet estimation and deconvolution of reflection seismic signals," *IEEE Trans. Geosci. Remote Sens.*, vol. 34, no. 2, pp. 377–384, Feb. 1996.
- [49] R. Buxton and L. Frank, "A model for the coupling between cerebral blood flow and oxygen metabolism during neural stimulation," *J. Cereb. Blood Flow Metab.*, vol. 17, no. 1, pp. 64–72, 1997.
- [50] M. Woolrich, M. Jenkinson, J. M. Brady, and S. Smith, "Constrained linear basis set for HRF modeling using variational Bayes," *Neuroimag.*, vol. 21, pp. 1748–1761, 2004.
- [51] C. P. Robert, *The Bayesian Choice*, Second ed, ser. Springer Texts in Statistics. New York: Springer Verlag, 2001.
- [52] T. Liu, L. Frank, E. C. Wong, and R. B. Buxton, "Detection power, estimation efficiency, and predictability in event-related fMRI," *Neuroimag.*, vol. 13, no. 4, pp. 759–773, 2001.
- [53] S. Gautier, J. Idier, A. Mohammad-Djafari, and B. Lavayssière, "Traitement d'échogrammes ultrasonores par déconvolution aveugle," in *Actes du 16e Colloq. GRETSI*, Grenoble, France, Sep. 1997, pp. 1431–1434.
- [54] Y.-L. You and M. Kaveh, "A regularization approach to joint blur identification and image restoration," *IEEE Trans. Image Process.*, vol. 5, no. 3, pp. 416–428, May 1996.
- [55] E. Gassiat, F. Monfront, and Y. Goussard, "On simultaneous signal estimation and parameter identification using a generalized likelihood approach," *IEEE Trans. Inf. Theory*, vol. 38, no. 1, pp. 157–162, Feb. 1992.
- [56] J. Idier, Y. Goussard, and A. Ridolfi, "Unsupervised image segmentation using a telegraph parameterization of Pickard random fields," in *Spatial Statistics. Methodological Aspects and Some Applications*, vol. 159, M. Moore, Ed., New York, 2001, pp. 115–140.

Salima Makni was born in Tunisia in 1979. She graduated from the École Supérieure des Communications, Tunis, Tunisia, in 2002 and received the D.E.A. degree in signal processing from the Université de Paris-sud, Orsay, France, in 2003. Since 2003, she has been pursuing the Ph.D. degree with the Service Hospitalier Frédéric Joliot, Commissariat à l'Énergie Atomique, Orsay.

Her general interests are signal processing and biomedical imaging. She is mainly concerned with functional magnetic resonance imaging (fMRI), and she focuses on new approaches that allow for a better comprehension of brain functions.

Philippe Ciuciu (M'02) was born in France in 1973. He graduated from the École Supérieure d'Informatique Électronique Automatique, Paris, France, in 1996 and received the D.E.A. and Ph.D. degrees in signal processing from the Université de Paris-sud, Orsay, France, in 1996 and 2000, respectively.

Since November 2000, he has held a postdoctoral position with the Service Hospitalier Frédéric Joliot, Commissariat à l'Énergie Atomique, Orsay, where, since November 2001, he has held a full research scientist position with the functional and anatomical neuroimaging unit. His research interests include spectral analysis and optimization, and presently, he focuses on the application of statistical methods and regularized approaches to functional brain imaging (fMRI).

Jérôme Idier was born in France in 1966. He received the diploma degree in electrical engineering from École Supérieure d'Électricité, Gif-sur-Yvette, France, in 1988 and the Ph.D. degree in physics from University of Paris-Sud, Orsay, France, in 1991.

Starting in 1991, he was with the Centre National de la Recherche Scientifique. He is currently with the Institut de Recherche en Communications et Cybernétique, Nantes, France. His major scientific interest are in probabilistic approaches to inverse problems for signal and image processing.

Jean-Baptiste Poline received the degree in biomathematics in 1991 and the Ph.D. degree in 1994.

Since then, he has been interested in functional brain imaging analyses. He is now with the Service Hospitalier Frédéric Joliot, Orsay, France, where he is responsible for the functional data analysis group.